Taylor & Francis
Taylor & Francis Group

Combustion Science and Technology

ISSN: 0010-2202 (Print) 1563-521X (Online) Journal homepage: www.tandfonline.com/journals/gcst20

Numerical Study of the Influence of Bed Stoking on Pyrolysis of a Polydisperse Bulk of Spherical Particles Using DEM/CFD

Nikoline Hilse, B. Jaeger, C. Hentschel, E. Illana, M. Schiemann & V. Scherer

To cite this article: Nikoline Hilse, B. Jaeger, C. Hentschel, E. Illana, M. Schiemann & V. Scherer (13 Mar 2026): Numerical Study of the Influence of Bed Stoking on Pyrolysis of a Polydisperse Bulk of Spherical Particles Using DEM/CFD, Combustion Science and Technology, DOI: 10.1080/00102202.2026.2642856

To link to this article: https://doi.org/10.1080/00102202.2026.2642856

Published online: 13 Mar 2026.

COMBUSTION SCIENCE AND TECHNOLOGY
https://doi.org/10.1080/00102202.2026.2642856

Taylor & Francis
Taylor & Francis Group

Numerical Study of the Influence of Bed Stoking on Pyrolysis of a Polydisperse Bulk of Spherical Particles Using DEM/CFD

Nikoline Hilse, B. Jaeger, C. Hentschel, E. Illana, M. Schiemann, and V. Scherer

Institute of Energy Plant Technology (LEAT), Ruhr University Bochum (RUB), Bochum, Germany

ABSTRACT

This study numerically investigates the influence of mechanical agitation on the pyrolysis behavior of a polydisperse particle bed. The bed consists of wooden spheres of three different diameters arranged in a cylindrical reactor. Bed agitation is achieved by three vertically oscillating stoking rings, while convective heat is supplied by preheated nitrogen flowing through the bed and radiative heat by a surrounding high-temperature cylindrical reactor wall. A coupled Discrete Element Method (DEM) and Computational Fluid Dynamics (CFD) approach is employed to resolve particle motion, heat transfer to the particles as well as intra-particle heat conduction and pyrolysis. The comparison between stationary and agitated bed configurations reveals that agitation significantly enhances temperature homogenization within the bed, thereby accelerating the overall pyrolysis process and increasing the mass loss rate. The magnitude of this enhancement, however, strongly depends on the initial particle arrangement. Segregation effects arising from particle size differences alter the local temperature fields and, consequently, the effective bulk conversion rate. The results emphasize that, for the design and optimization of industrial-scale grate systems, understanding the interplay between bed motion, segregation, and conversion is essential.

ARTICLE HISTORY
Received 28 January 2026
Accepted 23 February 2026

KEYWORDS
Pyrolysis; mechanical agitation; heat transfer; polydisperse particle bulk; DEM; CFD

Introduction

Grate firing systems are widely used for the thermochemical conversion of bulky solid fuels such as biomass pellets (Ahn and Jang 2018), wood chips (Zhang et al. 2010), and municipal waste (Al-Mansour and Zuwala 2010; Yin and Li 2017). Grate systems can be subdivided into fixed beds and grates that induce movement into the bed by stoking or conveying elements. Moving-grate designs are typically classified as forward acting, backward acting, or roller grates. The moving elements not only transport the fuel along the grate but also promote vertical mixing and segregation through periodic bed agitation (Simsek et al. 2012), thereby affecting local reaction rates and overall conversion efficiency (Buss et al. 2018).

The conversion of biomass and waste-based particles in stationary fixed beds has been a topic of intense experimental and theoretical research and significant knowledge is available (Shin and Choi 2000; Rönnbäck et al. 2001; Van Kessel et al. 2004; Yang et al. 2004; Bleckwehl 2010; Porteiro et al. 2010).

CONTACT Nikoline Hilse hilse@leat.ruhr-uni-bochum.de Institute of Energy Plant Technology (LEAT), Ruhr University Bochum (RUB), Universitätsstraße 150, Bochum 44780, Germany

Fixed bed combustion is characterized by the presence of thermally thick particles and the formation of a reaction front that propagates through the fuel bed. When combustion air is supplied from the bottom, the reaction front moves in counterflow to the direction of the air. The propagation characteristics of this reaction front have been studied experimentally, for example, by Shin and Choi (2000), Rönnbäck et al. (2001) and Porteiro et al. (2010). They defined three regimes with different reaction front velocities. In the oxygen-limited regime, the reaction front velocity increases with higher combustion air mass flow, as the reaction is constrained by oxygen availability. In the reaction-limited regime, sufficient oxygen is always present at the particle surface, resulting in the highest reaction front velocity. Finally, in the cooling-dominated regime at large combustion air mass flows, the reaction front velocity decreases because convective heat losses exceed the heat generated by the reaction. The effect of moisture content of the fuel (Yang et al. 2004), preheating of the fuel (Van Kessel et al. 2004), and particle shape (Bleckwehl 2010) on the reaction front propagation can be found in the literature. For pyrolysis, the situation simplifies as oxygen availability is no criteria, here it is solely the propagation of the temperature front through the bed that determines pyrolysis progress (Peters et al. 2003).

The numerical modeling of fixed bed conversion includes continuum-based approaches as, for example, described in (Van Der Lans et al. 2000) as well as DEM/CFD methods. DEM/CFD studies of fixed bed conversion have been reported, for example, in Wiese et al. (2016) for the combustion of wood pellets, in Peters et al. (2003) for pyrolysis of a bed of monodisperse spheres, in Gao X, Yu J, et al. (2021) for a bed of monodisperse cubical particles and in Mahmoudi AH, Hoffmann F, et al. (2016) for a bi-disperse fixed bed of spherical particles.

For moving, agitated beds, the situation becomes more complex, as the bed motion breaks up the reaction fronts described above, thereby influencing the progress of conversion within the bed. As a consequence of this complication, reaction progress on moving grates is far less understood. Previous studies on moving lab-scale grates without chemical reaction include investigations on particle mixing of monodisperse (Sudbrock et al. 2010) and mixing and segregation of polydisperse beds (Hilse et al. 2022), as well as on residence time distribution (Beckmann et al. 2002; Džiugys et al. 2007). Numerical studies on moving grate systems including thermochemical conversion of the solid material and gas-phase reaction are limited. Again, continuum-based approaches have been used, e.g. see Yang et al. (2004). However, these approaches can model mixing and segregation on grates only in a highly simplified manner. These effects can be better described by particle-based approaches such as the DEM. DEM/CFD studies on moving grates have been reported, for example in Mahmoudi AH, Besseron X, et al. (2016) for the combustion of a bed of monodisperse wood spheres or in Wissing et al. (2017) for the combustion of polydisperse bed of spherical municipal waste particles. Validation of such simulations is difficult, as measurements in the moving beds are difficult. An example for measurements in a 108 MWth biomass moving grate can be found in Yin and Li (2017).

Recent studies that combine DEM/CFD simulations and experiments have been presented on the combustion of straw pellets (Buss et al. 2019) and beech wood particles of different shapes (spheres, cylinders, cubes) (Buss et al. 2018) in a batch-operated stoker grate. These works demonstrated that particle motion significantly affects temperature uniformity, gas flow distribution, and overall reactivity in moving grate systems. The authors detected, for example, that volatile ignition above the pellet bed is

faster in the fixed bed compared to the agitated bed. Ignition of the volatiles also depends on particle shape. The higher the mobility of the particles in the bulk (spheres > cylinders > cubes), the larger the delay of ignition. Furthermore, mass loss rate of the bed after ignition is increased when the bed is stoked. Note that polydisperse particle assemblies were not examined.

Numerical studies on biomass conversion require models for both pyrolysis and char conversion. In this work, we focus on pyrolysis, for which many kinetic schemes are available. A comprehensive treatment of biomass-pyrolysis kinetics lies beyond the scope of the present study. For detailed discussions of reaction mechanisms, kinetic modeling approaches, and associated parameters, the reader is referred to the review articles Xia et al. (2021) and Diblasi (2008). Single-particle models describing the pyrolysis of solid particles were presented in Fan et al. (1978) and Babu and Chaurasia (2003), both integrating intra-particle heat and gas transport. Single-particle models for the pyrolysis of thermally thick particles, used in DEM/CFD simulations, can be found, for example, in Peters et al. (2003) or Jaeger et al. (2023). Whereas in Peters et al. (2003), spherical particles are used, in Jaeger et al. (2023) results for cubical and cylindrical particles are presented as well. An overview on models for particle shrinkage during pyrolysis or the prediction of detailed pyrolysis gas composition can be found in a recent review paper (Attanayake et al. 2023) on the modeling of pyrolysis using DEM/CFD.

DEM/CFD investigations focusing on pyrolysis in reactors with moving particles have been reported. Recent studies examined fluidized beds (Houston et al. 2022), entrained flow reactors (Gao et al. 2021) and rotary drums (Wang et al. 2022), with only the latter considering thermally thick particles. However, to the authors' knowledge, neither DEM/CFD simulations nor experimental studies have addressed pyrolysis on moving grates or its differences compared with fixed-bed pyrolysis. The present study addresses this gap by providing a DEM/CFD analysis of pyrolysis of thermally thick biomass particles on moving grates. By focusing solely on pyrolysis, the study isolates the mechanisms of thermal decomposition, heat transfer, and bulk particle movement, independent of subsequent gas-phase reactions, oxidation, or char combustion. The particle bed consists of wooden spheres of three different diameters arranged in a cylindrical reactor geometry. Agitation is provided by three vertically oscillating stoking rings, while heat is supplied via preheated nitrogen flow (convective) and a surrounding high-temperature cylinder wall (radiative). The main goal of this study is to systematically compare stationary and agitated configurations by (1) quantifying the effect of bed motion on temperature distribution and mass-loss rates and (2) assessing the role of particle size distribution on local conversion behavior.

Numerical model

DEM, CFD and coupling

Numerical simulations were performed with an in-house DEM code coupled with OpenFOAM. The DEM code integrates the equations for translational (1) and rotational (2) motion of the particles.

Table 1. Contact force parameters.

Coefficient of restitution [-]	Collision time [s]	κ [-]	Rolling friction coefficient [-]	Static friction coefficient [-]
0.61	5.0e-4	0.8	4.2e-4	0.29

$$m_i \frac{d^2\vec{x}_i}{dt^2} + \frac{dm_i}{dt}\frac{d\vec{x}_i}{dt} = \sum_{j=1}^{N} \vec{F}_{ij} + m_i\vec{g} \tag{1}$$

$$\theta_i \frac{d^2\vec{\varphi}_i}{dt^2} + \frac{d\theta_i}{dt}\frac{d\vec{\varphi}_i}{dt} = \sum_{j=1}^{N} \vec{M}_{ij} = \sum_{j=1}^{N} \left(\vec{r}_i \times \vec{F}_{ij} + \vec{M}_j^r\right) \tag{2}$$

The mass of the particle is given by m_i and its linear acceleration is described by $d^2\vec{x}_i/dt^2$. The change in momentum that occurs when the particle loses or gains mass is accounted for by $dm_i/dt\vec{x}_i/dt$. $\vec{F}_{ij}$ represents the external forces exerted by other particles or by the walls. In (2) θ_i denotes the particles moment of inertia and $d^2\vec{\varphi}_i/dt^2$ the angular acceleration. The change of the moment of inertia due to mass gain or loss of the particle is represented by $d\theta_i/dt \cdot d\vec{\varphi}_i/d$t. $\vec{M}_{ij}$ corresponds to the torques induced by contact with neighboring particles or wall, while $\vec{M}_j^r$ represents the rolling friction torque. Finally, $\vec{r}_i$ describes the distance from center of gravity to the contact point of particle/particle or particle/wall interaction. The parameters used to calculate the contact force in the spring-dashpot model are listed in Table 1. The DEM code also accounts for the equations governing intraparticle processes, which will be described later.

The CFD code used is *fireFoam* (OpenCFD Ltd 2024). It solves the momentum, energy and species conservation equation. The non-reacting gas phase in the reactor consists of N_2 as well as the gases that are released from the pyrolysis of the particles. Gas flow is assumed to be laminar. For brevity, we refrain from presenting the fluid equations here; they can be found, for example, in (Jaeger et al. 2023).

The simulations carried out in the present work employ an unresolved DEM/CFD approach, being the particles represented on the CFD side by a local porosity field derived from the DEM solver. The advantage of the unresolved method lies in its significantly reduced computational cost compared to resolved DEM/CFD simulations, which fully resolve the flow field around each particle.

In the unresolved approach, the Computational Fluid Dynamics (CFD) mesh is considerably coarser than in fully resolved simulations, with the cell size chosen to be in the same order of magnitude as the diameter of the particles within the computational domain. As individual particle geometries may extend beyond the boundaries of a single CFD cell, fluid variables and source terms are spatially distributed using a Gaussian kernel function that accounts for the particle's distance to neighboring cells to accurately capture the coupling between both phases (Kalderon et al. 2022). The exchange of heat, mass, and momentum between the particle and the gas phase is modeled through source term formulations implemented in *fireFoam* (FireFoam 2024). Further details on the CFD – DEM coupling framework used in this study can be found in (Brömmer et al. 2024).

The CFD mesh consists of approximately 75,000 cells (see APPENDIX Figure A1). The control volumes surrounding the particle bulk have a characteristic length of 0.0137 m, which

Table 2. Mesh data and time steps for DEM/CFD.

	Surface elements	Number of cells	Time step [s]
Sphere, Ø 6 mm	242	281	–
Sphere, Ø 10 mm	348	743	–
Sphere, Ø 20 mm	666	1716	–
CFD mesh	–	75.255	–
CFD	–	–	2.5e-3
DEM	–	–	1.0e-5

is slightly smaller than the diameter of the largest particle (Ø 20 mm). This cell size ensures an adequate resolution of the reactor geometry relative to the mean particle diameter.

Further details on CFD and intraparticle mesh and computing time steps for DEM and CFD can be found in Table 2.

Heat transfer

Heat transfer in the packed bed occurs through convection, contact between particles and particles as well as between particles and walls, and by radiation.

For convection, the heat transfer coefficient $\bar{\alpha}$ is determined according to (3):

$$\bar{\alpha} = \frac{Nu\lambda_f}{d_p}, \tag{3}$$

where Nu is the Nusselt number, d_p is the diameter of the particle and λ_f is the thermal conductivity of the fluid. Using the Gnielinski correlation (Gnielinski 1975), the Nusselt number for a single particle is calculated as a function of the Reynolds number Re and the Prandtl number Pr from

$$Nu_p = 2 + 0.644 * Re^{1/2} * Pr^{2/3}, \tag{4}$$

Note that the turbulent contribution Nu_{turb} was omitted in (4) for simplicity. The increased heat transfer in packed beds is considered by the local porosity Φ:

$$Nu = f_\Phi * Nu_p = [1 + 1.5 * (1 - \Phi)] * Nu_p. \tag{5}$$

Contact heat transfer is accounted for by the model of Vargas and McCarthy (Vargas and McCarthy 2001, 2002). The model consists of two parts: the direct heat transfer through the contact point of the two solids expressed by the contact conductivity H_c and the heat transferred through the stagnant gas layer in the vicinity of the contact point, expressed by the gas conductivity H_g. The total heat transferred reads as:

$$\dot{Q} = (H_c + H_g)\Delta\mathrm{T}. \tag{6}$$

The contact conductivity can be calculated by Equation (7) where a_c, the contact radius, is given by the Hertz theory (Hertz 1882). The thermal conductivity used is the harmonic mean λ_{harm} of the two materials:

$$H_C = 2\lambda_{harm} \cdot a_c. \tag{7}$$

The gas conductivity H_g is calculated from the reciprocal of the thermal resistance with the area exposed to the gas A_g, the thermal conductivity of the gas λ_g and the averaged

length l_g over which the heat flux applies. For a more detailed description of the contact heat transfer model, see (Hilse et al. 2023).

$$H_g = \frac{\lambda_g A_g}{l_g} \tag{8}$$

Radiative heat transfer to the particles is modeled with the Discrete Ordinates Method (DOM). The model calculates the incident radiation G within the domain while considering particle contribution through the local number of particles, particle size, temperature and local bed porosity Φ. The specific heat flux $\dot{q}_{rad}$ due to radiative heating is calculated by:

$$\dot{q}_{rad} = \varepsilon_{surf} \emptyset \left(\frac{G}{4} - \sigma T_{surf}^4 \right), \tag{9}$$

where the emissivity of the particle ε_{surf} is set to 0.85. Details of the integration on the DOM into the present DEM/CFD framework can be found in (Jaeger 2024).

Note that the heat fluxes calculated with the above equations are distributed among the individual surface elements of the particles according to the surface area A_i of each element.

Intraparticle processes

Heat and mass transport, along with particle pyrolysis, is computed on a particle-internal tetrahedral mesh. Particles are assumed to be completely dry. For pyrolysis, three components are considered here: solid biomass, solid char and gaseous volatiles. Solid and gaseous components are assumed to be in thermal equilibrium. To represent the thermodynamic properties of beech wood, the density was set to 700 kg/m^3. Char and volatiles account for 97% of the particles mass, leaving 3% ash content.

Assuming a zero enthalpy of pyrolysis, the transport equations for energy (10) and volatiles' mass (11) are:

$$\frac{\partial \left(\rho c_p T\right)_{eff}}{\partial t} = \vec{\nabla} \cdot \left(\lambda_{eff} \vec{\nabla} T_{eff} \right) + S_Q, \tag{10}$$

$$\frac{\partial \rho_{vol}}{\partial t} = \vec{\nabla} \cdot \left(D_{vol,eff} \vec{\nabla} \rho_{vol} \right) + S_{vol} - S_{vol,CFD}, \tag{11}$$

where the subscript *eff* denotes the effective diffusion coefficient or temperature of a particle cell. The heat source/sink at the particle surface is described by S_Q. $S_{vol,CFD}$ is the rate of volatiles released inside the particle.

$$S_{vol} = m_{biomass} \cdot k_{vol} \cdot exp \frac{-E_{vol}}{R_m T_{eff}} \tag{12}$$

In parallel, solid biomass is converted to char, which remains as a solid matrix and is described by S_{char} given by Equation (13):

$$S_{char} = m_{biomass} \cdot k_{char} \cdot exp \frac{-E_{char}}{R_m T_{eff}} \tag{13}$$

The kinetic model was previously used by Babu et al. (Babu and Chaurasia 2003) and the values k_{vol}, E_{vol} and k_{char}, $E_{char}$are given in Sadhukhan et al. (2008). The kinetic data is based on Casuarina (beech) wood. All kinetic pyrolysis parameters used are listed in Table 3.

$S_{vol,CFD}$, in Equation (11), represents the mass flow of volatiles transferred through the boundary layer with β being the mass transfer coefficient:

$$S_{vol,CFD} = \beta\left(\frac{dm_{vol}}{dt}\right). \tag{14}$$

The mass of biomass is assumed to be homogeneously distributed in the particle. No more gaseous volatiles are formed (S_{vol}, Equation 12) as soon as the mass of biomass inside a cell reaches zero. The same applies to char production (S_{char}, Equation 13). The effective specific heat capacity and thermal conductivity (see. Equation 10) depend on the amount of biomass, char and volatiles present in the cell. They are weighted by the mass fraction Y_i of these components:

$$c_{p,eff} = (1 - Y_{vol})c_{p,solid} + Y_{vol}c_{p,vol} \tag{15}$$

$$\lambda_{eff} = (1 - Y_{vol})\lambda_{solid} + Y_{vol}\lambda_{vol} \tag{16}$$

with

$$Y_{vol} = \frac{m_{vol}}{m_{solid} + m_{vol}}. \tag{17}$$

The properties of the solid are in turn weighted by the local mass of biomass and char

$$c_{p,solid} = Y_{biomass}c_{p,biomass} + Y_{char}c_{p,char} \tag{18}$$

$$\lambda_{solid} = Y_{biomass}\lambda_{biomass} + Y_{char}\lambda_{char} \tag{19}$$

With $Y_{biomass}$and Y_{char}being:

$$Y_{biomass} = \frac{m_{biomass}}{m_{solid}} \tag{20}$$

$$Y_{char} = \frac{m_{char}}{m_{solid}} \tag{21}$$

Heat capacity of solids and volatiles as well as the effective diffusivity of volatiles are also listed in Table 3.

Table 3. Parameters pyrolysis model.

	Biomass	Char	Volatiles	Ash	Unit
Pre-Exponential Factor	–	13.20	168.4	–	1/s
Activation Energy	–	45960	51965	–	J/(mol K)
Heat Capacity	f(T)[1]	2100	f(T)*	1000	J/(kg K)
Thermal Conductivity	f(T)[2]	0.1	f(T)*	0.1	W/(m K)
Effective Diffusivity	–	–	1.0e-2	–	m^2/s

f(T)[1] $= 1500 + T$, with T in °C (Grønli and Melaaen 2000).
f(T)[2] $= 0.13 + 0.0003 * T$, with T in °C (Wenzl 1970).
*polynomial data from NIST/CHEMKIN.

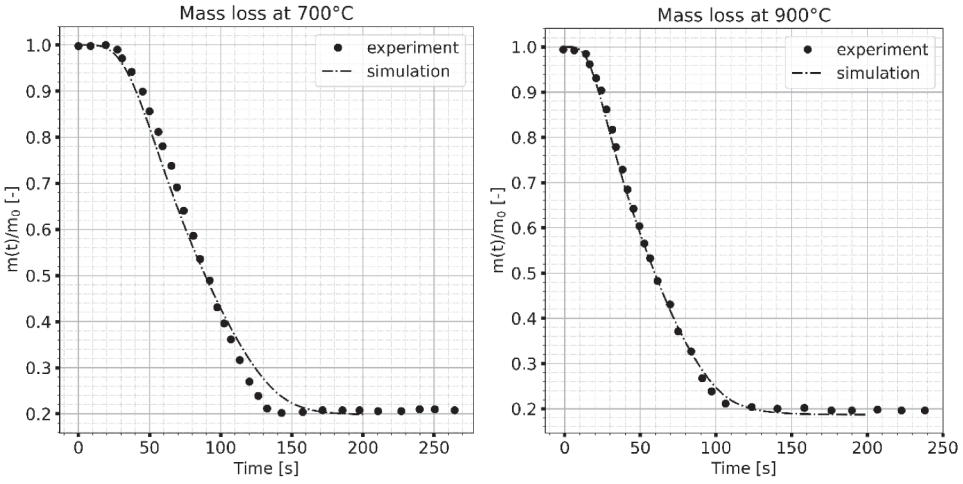

a. Comparison of the normalized mass loss as a function of time at 700°C

b. Comparison of the normalized mass loss as a function of time at 900°C

Figure 1. (a) Comparison of the normalized mass loss as a function of time at 700°C. (b) Comparison of the normalized mass loss as a function of time at 900°C.

Model validation

The single-particle model was validated against experimental data in (Behling 2016). Pyrolysis experiments of thermally thick, spherical beech wood particles with a diameter of 0.02 m were performed in the Large-scale Oven for Kinetics Investigation (LOKI) test facility. The particle is water free and has a density is 700 kg/m^3. Mass loss was recorded during the pyrolysis process at 700°C and 900°C

The normalized mass loss ($m(t)/m_0$) of the single particle given in Figure 1(a,b) shows good agreement between experimental data and simulation. Just the 700°C case differs slightly at the end of the pyrolysis process (simulation underestimating the mass loss rate between 100 s and 160 s).

Numerical set up

The model of the pyrolysis reactor consists of a burner bowl enclosed within a cylindrical casing. The burner bowl is filled with spherical particles of three sizes up to a filling height of 50 mm. The particle diameters are 6 mm (1083 particles), 10 mm (602 particles) and 20 mm (70 particles).

Two configurations are examined (see Figure 2). In configuration 1, the particles are arranged in layers according to size: the largest spheres are placed at the bottom, followed by the medium-sized spheres in the middle and the smallest spheres on top. Configuration 2 represents a random distribution of particles within the burner bowl. When the particle bed is agitated, both configurations exhibit a distinct segregation of particle sizes. After 400 s of simulated time, the final arrangement shown in Figure 2, is achieved. The smallest particles have predominantly settled at the bottom of the particle bed, the medium-sized particles are mainly concentrated in the middle region and the

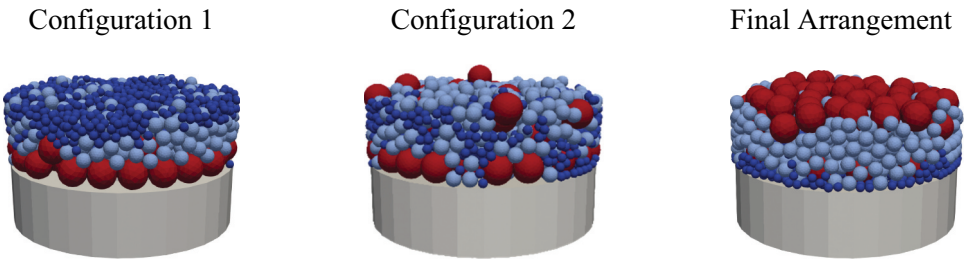

Figure 2. Particle arrangements. Left: configuration 1 (layers according to size), middle: configuration 2 (random distribution), right: final arrangement.

largest particles migrate upward, accumulating near the top of the bulk. This segregation behavior corresponds to the well-known Brazil Nut Effect (Hong et al. 2001), where larger particles rise to the surface of a vibrated or agitated granular medium. The capability of the in-house DEM code to predict such behavior accurately was shown in Hilse et al. (2022), where segregation simulations were compared are against experiments.

The bottom of the burner bowl is formed by three circular-shaped elements (see Figure 3). The inner cylindrical element has a diameter of 52 mm and is surrounded by two ring-shaped elements with a width of 26 mm each. While the middle ring remains stationary, the inner cylinder and the outermost ring are repeatedly moved up and down at a speed of 0.04 m/s with a stroke length of 20 mm. A detailed schematic diagram of the reactor geometry and numerical set up can be found in the APPENDIX (A1–A4).

Nitrogen at a temperature of 973 K is introduced into the system from the bottom with a velocity of 0.1 m/s, flowing upward through the particle bed. The burner bowl is maintained at a constant temperature of 973 K, while the reactor walls above the particle bed are kept at a fixed temperature of 1273 K. Each simulation run covers a total time of 400 s.

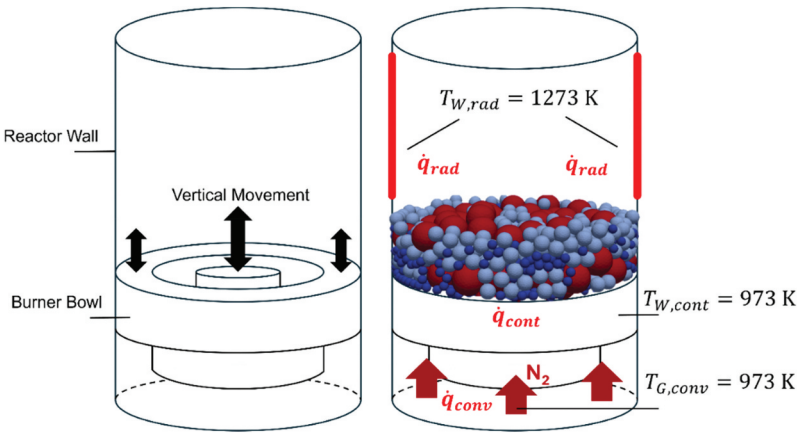

Figure 3. Scheme of the reactor set up.

Results and discussion

As an indicator of the pyrolysis progress, the rate of the normalized mass of the particle bulk defined in (22) is used, where $m(t)$ denotes the mass of the particle bulk at the time t, m_0 is the initial mass at $t = 0$, and Δt is the time step size.

$$\frac{d}{dt}\left(\frac{m(t)}{m_0}\right) = \frac{\left[\frac{m(t)}{m_0} - \frac{m(t+\Delta t)}{m_0}\right]}{\Delta t} \tag{22}$$

Figure 4 shows the mass loss rate of the particle bulk over time for configuration 1 (Figure 4a) and configuration 2 (Figure 4b). The solid lines represent the stationary cases, while the dashed lines correspond to the agitated cases. The final normalized mass loss for the particle bulk is 0.205.

For configuration 1, the stationary case (Figure 4a) reaches its maximum mass loss rate of 4.6e-3 after 120 s. The rate subsequently decreases, reaches a saddle point at 170 s (3.7e-3), and approaches zero after 370 s. The mass loss rate of the agitated case increases until it reaches its peak of 6.8e-3 at 135 s, after which it steadily decreases to zero after 310 s. For configuration 2 (Figure 4b), the agitated case delivers very similar results to those of the agitated case of configuration 1. The results for the stationary cases, however, differ significantly. For configuration 2, the mass loss gradient does not exhibit the saddle point observed for configuration 1. Instead, it shows a steady increase followed by a continuous decrease. The maximum rate is higher compared to configuration 1, approximately 5.6e-3, and the reaction is finished earlier, after 340 s. For both configurations, the rates increase slightly faster in the stationary cases than in the agitated cases within the first 50–100 s, indicating an earlier onset of the pyrolysis reaction. The reason for this behavior is discussed further below, based on the results for the individual particle sizes.

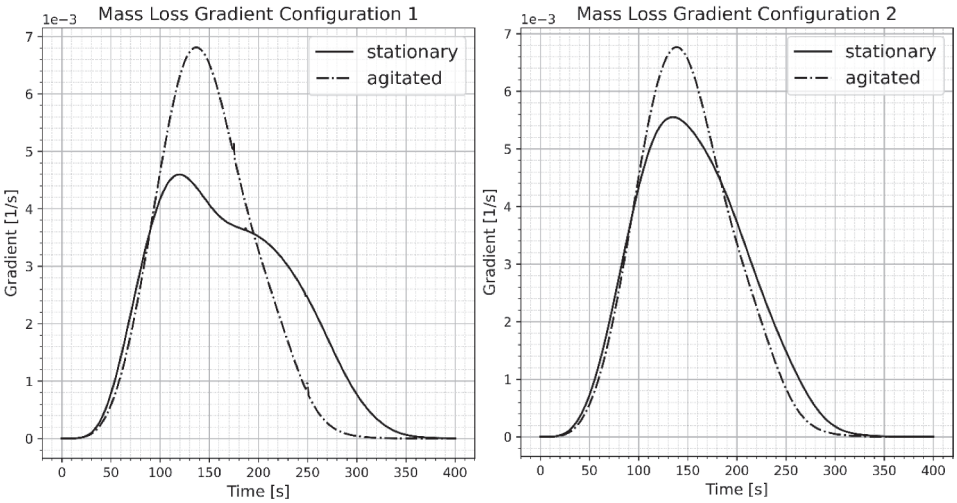

a. Mass loss gradient over time, configuration 1

b. Mass loss gradient over time, configuration 2

Figure 4. (a) Mass loss gradient over time, configuration 1. (b) Mass loss gradient over time, configuration 2.

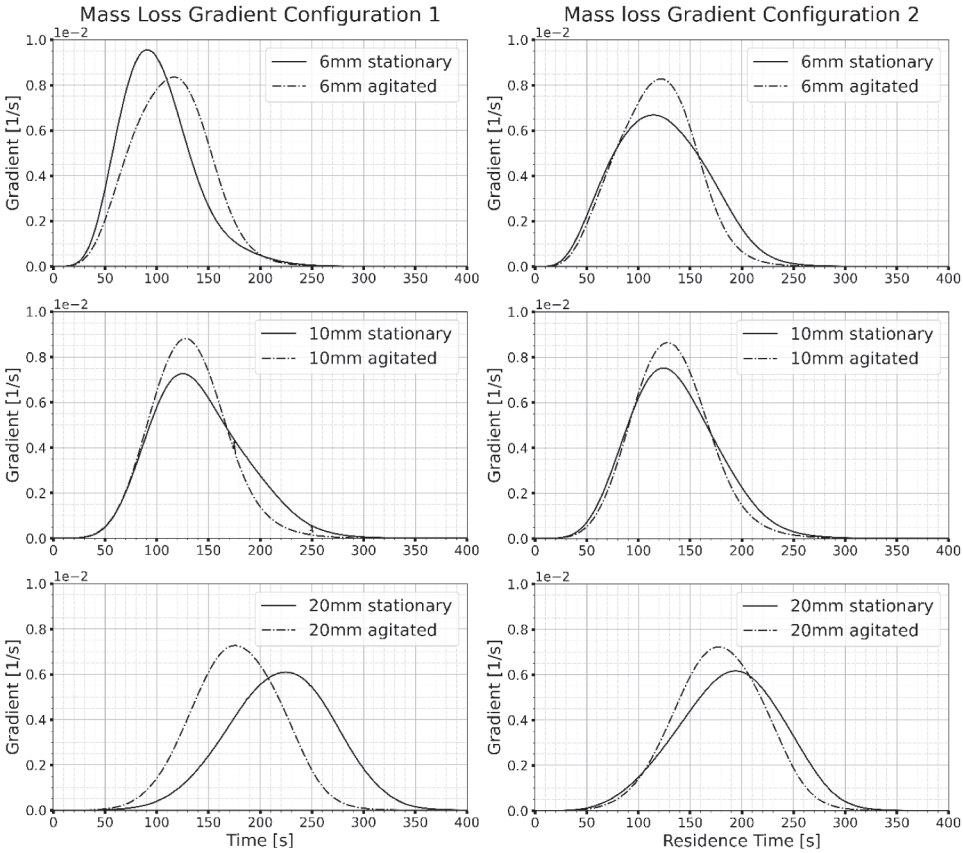

a. Mass loss gradient over time for configuration 1, top: 6 mm particles, middle: 10 mm particles, bottom: 20 mm particles

b. Mass loss gradient over time for configuration 2, top: 6 mm particles, middle: 10 mm particles, bottom: 20 mm particles

Figure 5. (a) Mass loss gradient over time for configuration 1, top: 6 mm particles, middle: 10 mm particles, bottom: 20 mm particles. (b) Mass loss gradient over time for configuration 2, top: 6 mm particles, middle: 10 mm particles, bottom: 20 mm particles.

Figure 5(a) shows the individual rates of the normalized mass for each particle size in configuration 1. As expected, the 6 mm particles, mostly forming the upper layer, begin to react first (at approximately 35 s) because they are located closest to the radiative heat source (1273 K) at the surrounding walls above the particle bed. This early onset of the pyrolysis reaction regarding the smallest particles explains why the overall mass loss rates depicted in Figure 4 increase more rapidly at the beginning in the stationary case compared with the agitated bed. In contrast to the overall particle assembly (Figure 4a), the pyrolysis progression of the 6 mm particles remains faster in the stationary case than in the agitated one throughout almost the entire simulation. The mass loss rate reaches its maximum about 5 s earlier in the stationary case. Although the agitated case exhibits a slower increase and a lower peak value, both curves approach zero at roughly the same time, after about 260 s. Although the mass loss rates increase initially faster in the static case, progression toward the final state is

delayed compared to the agitated bed by non-moving 6 mm particles located below the surface layer, which receive less radiative heat.

In the stationary case, the 10 mm and 20 mm particles begin to react approximately 35 s and 135 s later, respectively, than the 6 mm particles. For these larger particle sizes, the agitated cases exhibit higher maximum mass loss rates than the stationary cases. Moreover, the final state is reached earlier for the agitated case for both the 10 mm and 20 mm particles, consistent with the trends observed for the overall particle assembly in Figure 4.

The comparison of all three particle sizes shows that the lower the particle is located within the bulk, the larger the time difference between agitated and stationary case in reaching the final state. Therefore, the 20 mm particles exhibit the largest deviation between agitated and stationary cases. For the static case, where the particle bulk remains in its initial arrangement, the 20 mm particles in the bottom layer require approximately 100 s additional time compared to the medium-sized particles to reach the peak in mass loss rate. This delay causes the saddle point for the curve of the stationary case in Figure 4(a).

A comparison with configuration 2, shown in Figure 5(b), indicates that the agitated cases for both configurations do not exhibit significant differences. The curve of the stationary case for the 6 mm particles reveals that these small particles now react slower than in configuration 1, as they are partially located below the surface layer, therefore, receiving less radiative heat. The 10 mm particle curves are similar to configuration 1, although the stationary case reaches steady state slightly faster. The most pronounced difference is observed for the 20 mm particles. The curve reaches the final state after 325 s, which is almost 50 s earlier than in configuration 1, as some of the 20 mm particles now are exposed to direct radiation in the surface layer.

The differences in the mass loss rate curves result from height-dependent temperature evolution of the particle bed. To analyze the variance of bulk temperature, the particle assembly is divided into three horizontal layers, as illustrated in Figure 6. The bottom layer and the middle layer each have a fixed thickness of 0.02 m. The top layer forms the upper boundary of the particle bed and has no fixed thickness, since the total bed height varies during agitation.

Figure 7(a,b) present the bulk-averaged temperatures of these three layers both for the stationary cases (top) and the agitated cases (bottom). In the stationary cases, the average temperature decreases with decreasing height within the bed. This trend results from the lower temperatures in the bottom region, approximately 300 K below the upper section,

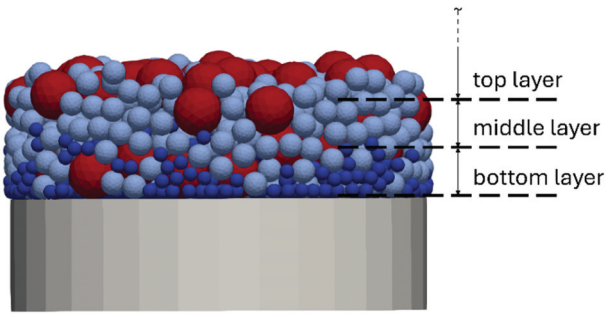

Figure 6. Division of the particle bed in three height layers.

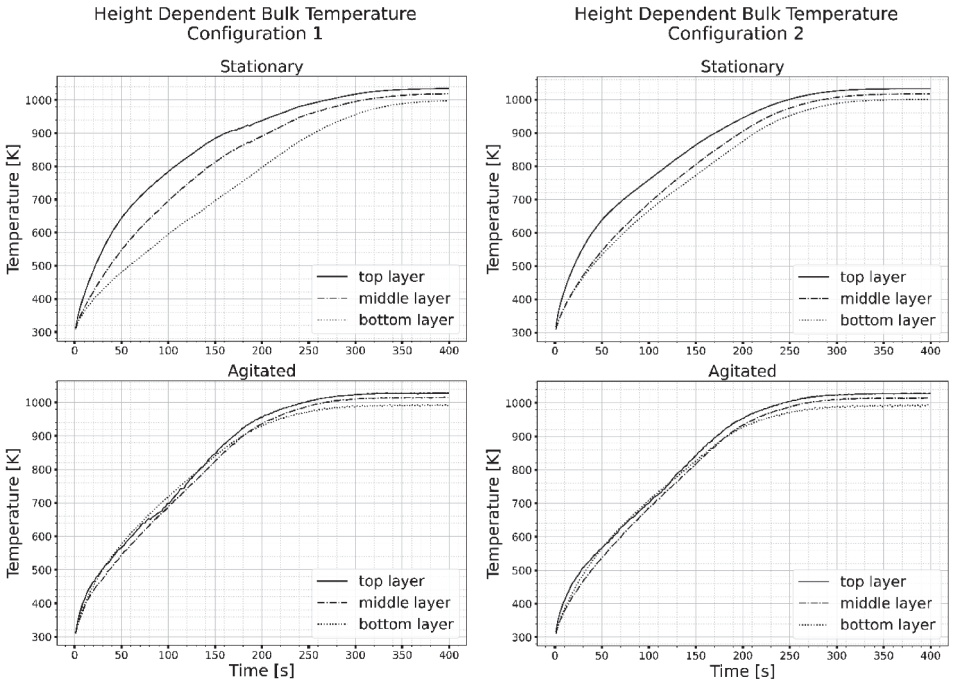

a. Temperature development over bulk height for configuration 1 (top: stationary, bottom: agitated)

b. Temperature development over bulk height for configuration 2 (top: stationary, bottom: agitated)

Figure 7. (a) Temperature development over bulk height forconfiguration 1 (top: stationary, bottom: agitated). (b) Temperature development over bulk height forconfiguration 2 (top: stationary, bottom: agitated).

Table 4. Average particle diameter in height levels.

	Configuration 1 – Stationary, average particle diameter [m]	Configuration 2 – Stationary, average particle diameter [m]
Top layer	0.0068	0.0086
Middle layer	0.0082	0.0077
Bottom layer	0.0127	0.0078

caused by the presence of the nitrogen flow and the burner bowl wall both maintained at 973 K, compared with the radiating wall in the upper part of the reactor, which is at 1273 K.

It appears that the bottom layer exhibits significantly faster heating in configuration 2 (Figure 7a, top) than in configuration 1 (Figure 7b, top). This behavior can be attributed to the different particle size distributions within the layers of the two configurations. Table 4 lists the average particle diameters of the three layers for the stationary cases. The mean particle diameter in the bottom layer of configuration 1 is approximately 1.6 times larger than in configuration 2. The higher mass of larger particles results in a lower rate of temperature increase.

For comparison, Figure 8 shows the surface temperature distribution of the particle bed for configurations 1 and 2 after 200 s of simulated time. It is clearly visible that the particles

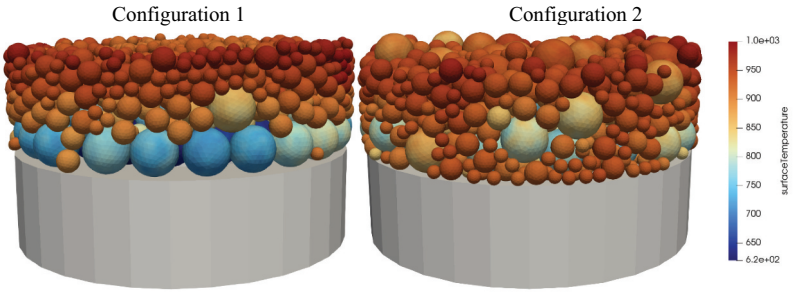

Figure 8. Temperatures of the stationary particle bulk at 200 s simulation time. Left: configuration 1, right: configuration 2, temperature scale from 620 to 1000 K.

in the bottom layer exhibit lower temperatures in configuration 1 than in configuration 2. It can be concluded that the temperature development of the bulk layers is influenced by the particle size composition. Once steady-state conditions are reached, both configurations show the same general temperature stratification: the top layer exhibits the highest temperatures, being closest to the radiation source, the heated reactor walls above the bed, while the temperature in the middle layer is approximately 20 K lower, and the bottom layer again about 50 K lower than the middle layer.

For the agitated cases (Figure 7a,b, bottom), the temperature differences between the layers are considerably smaller than in the stationary cases. Particle mixing promotes a more homogeneous heat distribution throughout the bed. Nevertheless, toward the end of the simulation, when steady-state temperatures are reached, a slight temperature gradient from top to bottom layer remains. This results from the initial temperature gradient in the reactor and inhibited particle mixing caused by segregation effects.

The temperature gradients along the bed height also lead to layer-dependent differences in the particles' mass loss over time. For configuration 1, this is shown in Figure 9(a,b). It depicts the median of the normalized mass $m(t)/m_0$ over time for all particles of a given particle size in the system (solid line). The shaded gray area represents the range between maximum and minimum values.

Due to the pronounced temperature stratification in the system, the reaction times of the particles vary significantly depending on the layer in which they are located. Since the arrangement is not perfectly separated and smaller particles fell through gaps between other particles into lower layers, large differences in reaction rates also occur among particles of the same size. Further on the comparison reveals that keeping the particle bulk stationary (Figure 9a) results in a substantially wider spread of reaction time within particles of the same size compared to the agitated case (Figure 9b). Agitation affects the particle bulk in two major ways. In the beginning of the process, the mixing of the particle bed continuously moves particles between layers, exposing them to different temperature levels. Then contact-based heat transfer allows particles of higher temperature to pass thermal energy to particles at lower temperature. This homogenizes the heating of the particles and thus reduces the variance in their pyrolysis rates, and hence leads to smaller spread in the particle masses as observed in Figure 9(b). Second, at later stages particle size segregation causes larger particles, which have longer reaction times due to their larger mass, to remain predominantly in the upper layers of the bed. The higher temperatures promote faster

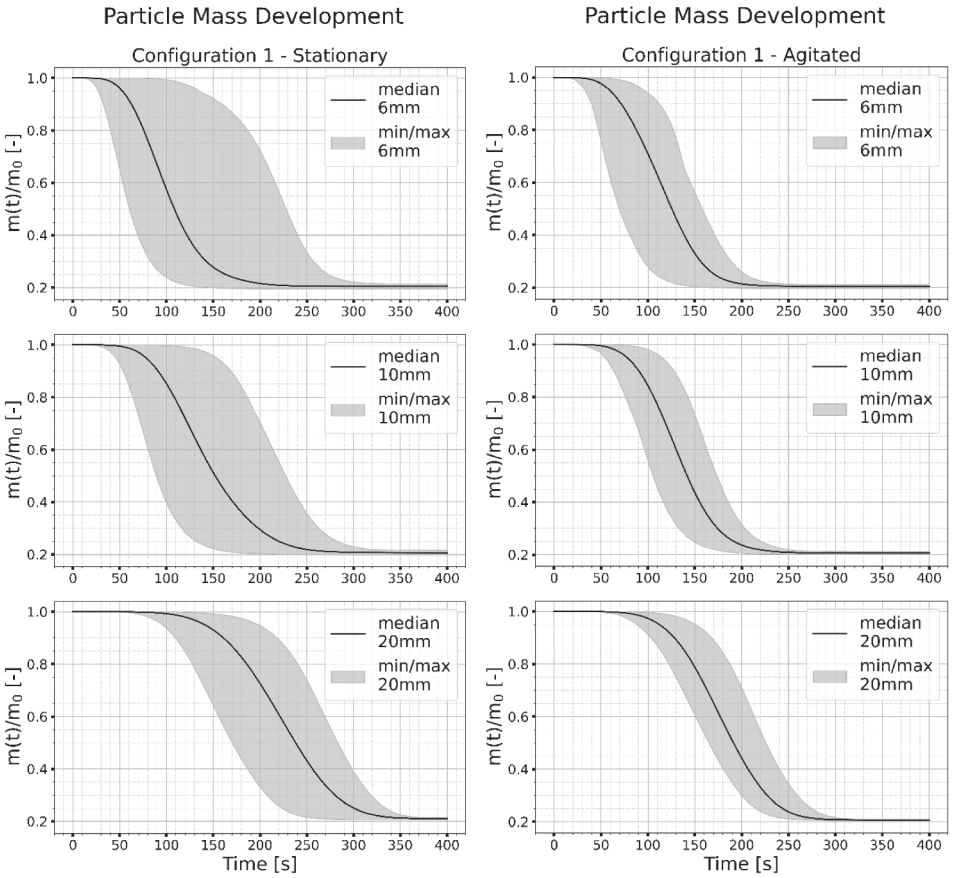

a. Particle mass ratio over time for configuration 1, stationary,

b. Particle mass ratio over time for configuration 1, agitated

Figure 9. (a) Particle mass ratio over time for configuration 1, stationary. (b) Particle mass ratio over time for configuration 2, stationary.

reactions. This results in an overall acceleration of the bed's reaction as evidenced by comparison of Figure 9(a,b): for all particle sizes, the agitated case in Figure 9(b) reaches the terminal particle mass earlier than in Figure 9(a).

The same effects can be observed for configuration 2. However, due to the altered positioning of the particles, the reaction rates in the stationary case diverge less than in configuration 1. For completeness, the curves of absolute mass over time for configuration 2 are provided in the APPENDIX (Figure A5).

Finally, Figure 10 shows the mass loss rate of the particle bulk for the final arrangement as depicted in Figure 2. Even in the segregated state, the agitation of the packed bed continues to slightly influence and accelerate the pyrolysis process.

Summary

The process of particle pyrolysis is compared for fixed and agitated beds using a coupled Discrete Element Method (DEM) and Computational Fluid Dynamics (CFD) simulation

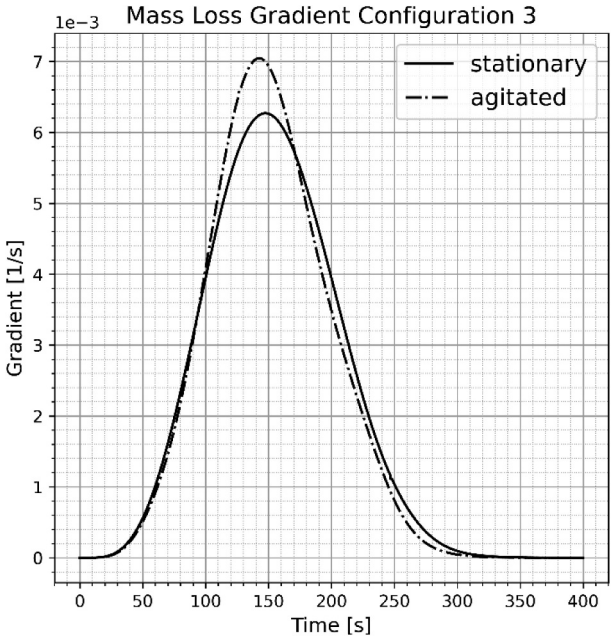

Figure 10. Mass loss rate over time for configuration 3, segregated particle arrangement.

framework. The numerical simulations were performed with an in-house DEM code coupled with OpenFOAM, while the interaction between the discrete particle phase and the surrounding fluid is modeled using the non-resolved DEM/CFD approach. The modeled single particle pyrolysis is validated against experimental data. The simulated system consists of a cylindrical particle bed with a height of 50 mm, composed of spherical particles with diameters of 6 mm, 10 mm, and 20 mm. Heating of the bed occurs through radiation from hot cylindrical reactor walls above the bed (1273 K) and convection from a nitrogen flow at 973 K entering the bed from the bottom. The bed could be agitated by three vertically moving stoking rings.

Two initial arrangements were investigated: (i) a vertically size-graded configuration with the 6 mm particle at the top, the 10 mm particles in the middle, and the 20 mm particles at the bottom of the bed as well as (ii) a randomly mixed configuration. Both arrangements were analyzed with and without agitation. For agitation, the stroke length was set to 20 mm at a stroke velocity of 0.04 m/s.

For the stationary cases, pronounced temperature gradients develop along the bed height. These gradients are reduced when larger particles are positioned in the upper layers, where higher temperatures prevail in the reactor, while smaller particles occupy the lower layers, where the temperatures in the reactor are smaller. Comparison with the agitated cases reveals that bed motion increases the overall mass loss rate and promotes a more homogeneous temperature distribution within the bed. Consequently, the pyrolysis process proceeds faster, and the reaction times of the different particle sizes become more uniform. At longer agitation times, however, particle size segregation becomes increasingly pronounced, reducing the mixing efficiency and gradually reestablishing vertical temperature layering.

Overall, the results demonstrate that both the initial particle arrangement and bed agitation significantly affect the local temperature distribution and reaction progress during pyrolysis. To further generalize these findings, additional simulations are required that vary the thermal boundary conditions, stroke length, agitation frequency, and agitation sequence. Furthermore, future studies should incorporate particle shrinkage into the numerical model, as the reduction in particle size during pyrolysis influences the local porosity, interparticle contact dynamics, and heat-transfer pathways within the bed.

Nevertheless, the present study already provides valuable insights for practical reactor applications, clearly highlighting the strong influence of particle-bed mixing on reaction uniformity and overall pyrolysis performance in technical-scale systems.

Nomenclature

A	Area
a	Contact radius
c_p	Heat capacity
D	Effective diffusivity
E	Activation energy
F	Force
G	Incident radiation
H	Conductivity
k	Pre-exponential factor
m	Mass
λ	Thermal conductivity
$\dot{Q}$	Heat flux
$\dot{q}$	Specific heat flux
R	Gas constant
S	Source term
T	Temperature
t	Time
V	Volume
Y	Mass fraction
β	Local mass transfer coefficient
θ	Moment of inertia
ε	Emissivity
ρ	Density
σ	Stefan-Boltzmann constant
Φ	Porosity
Subscripts	
c	Contact
g	Gas
$harm$	Harmonic
m	Molar
rad	Radiation
$surf$	Surface
vol	Volatiles

Abbreviations

CFD	Computational Fluid Dynamics
DEM	Discrete Element Method
DOM	Discrete Ordinates Model

Disclosure statement

No potential conflict of interest was reported by the author(s).

Funding

This work has been funded by the Deutsche Forschungsgemeinschaft (DFG, German Research Foundation) [422037413]–CRC/TRR 287 "BULK-REACTION".

References

Ahn J, Jang JH. 2018. Combustion and heat transfer characteristics in a combustion chamber of a 13-step grate wood pellet firing boiler. J Mech Sci Technol. 32(3):1033–1040. https://doi.org/10.1007/s12206-018-0204-y

Al-Mansour F, Zuwala J. 2010. An evaluation of biomass co-firing in Europe. Biomass Bioenerg. 34(5):620–629. https://doi.org/10.1016/j.biombioe.2010.01.004

Attanayake DD et al. 2023. Review of modelling of pyrolysis processes with CFD-DEM. Flow Turbul Combust. 111(2):355–408. https://doi.org/10.1007/s10494-023-00436-z

Babu BV, Chaurasia AS. 2003. Modeling for pyrolysis of solid particle: Kinetics and heat transfer effects. Energy Convers Manag. 44(14):2251–2275. https://doi.org/10.1016/S0196-8904(02)00252-2

Beckmann M et al. 2002. Residence time behavior of waste in rotary kiln systems - experimental investigations and mathematical modelling. The Future of Waste Management in Europe, Düsseldorf. Strasbourg (FR): VDI Gesellschaft Verfahrenstechnik und Chemieingenieurwesen. p. 252–255.

Behling J. 2016. Untersuchungen zum thermischen umsetzungsverhalten von makroskopischen einzelpartikeln aus Holz. Ruhr-Universität Bochum.

Bleckwehl S. 2010. Charakterisierung der verbrennungstechnischen eigenschaften fester brennstoffe im festbett. KIT.

Brömmer M, Scharnowski M, Illana Mahiques E, Wirtz S, Scherer V. 2024. Investigating the inflow into a granular bed using a locally resolved method. Particuology. 85:89–101. https://doi.org/10.1016/j.partic.2023.03.022

Buss F, Wirtz S, Scherer V. 2018. Influence of stoking on the combustion of beech wood particles of different shape in an agitated bed. Exp Therm Fluid Sci. 95:27–34. https://doi.org/10.1016/j.expthermflusci.2018.01.009

Buss F, Wirtz S, Scherer V. 2019. Combustion of straw pellets in an agitated fuel bed: Experiments and DEM/CFD simulations. Combust Sci Technol. 194(1):195–212. https://doi.org/10.1080/00102202.2019.1678844

Diblasi C. 2008. Modeling chemical and physical processes of wood and biomass pyrolysis. Prog Energy Combust Sci. 34(1):47–90. https://doi.org/10.1016/j.pecs.2006.12.001

Džiugys A, Peters B, Hunsinger H, Krebs L. 2007. Experimental and numerical evaluation of the transport behaviour of a moving fuel bed on a forward acting grate. Granular Matter. 9(6):387–399. https://doi.org/10.1007/s10035-007-0064-0

Fan L, Fan LT, Tojo K, Walawender WP. 1978. Volume reaction model for pyrolysis of a single solid particle accompanied by a complex reaction. Can J Chem Eng. 56(5):603–609. https://doi.org/10.1002/cjce.5450560514

Gao X et al. 2021. Assessment of a detailed biomass pyrolysis kinetic scheme in multiscale simulations of a single-particle pyrolyzer and a pilot-scale entrained flow pyrolyzer. Chem Eng-New Y J. 418:129347. https://doi.org/10.1016/j.cej.2021.129347

Gao X, Yu J, Lu L, Rogers WA. 2021. Coupling particle scale model and superDEM-CFD for multiscale simulation of biomass pyrolysis in a packed bed pyrolyzer. AlChE J. 67(4):e17139. https://doi.org/10.1002/aic.17139

Gnielinski V. 1975. Berechnung mittlerer wärme- und stoffübergangskoeffizienten an laminar und turbulent überströmten einzelkörpern mit hilfe einer einheitlichen gleichung. Forsch Ing-Wes. 41 (5):145–153. https://doi.org/10.1007/BF02560793

Grønli MG, Melaaen MC. 2000. Mathematical model for Wood PyrolysisComparison of experimental measurements with model predictions. Energy Fuels. 14(4):791–800. https://doi.org/10.1021/ef990176q

Hertz H. 1882. Ueber die Berührung fester elastischer Körper. p. 156–171. https://doi.org/10.1515/crll.1882.92.156

Hilse N et al. 2023. Discrete element simulations of contact heat transfer on a batch-operated single floor of a multiple hearth furnace. Processes. 11(12):3257. https://doi.org/10.3390/pr11123257

Hilse N, Kriegeskorte M, Illana E, Wirtz S, Scherer V. 2022. Mixing and segregation of spheres of three different sizes on a batch stoker grate: Experiments and discrete element simulation. Powder Technol. 400:117258. https://doi.org/10.1016/j.powtec.2022.117258

Hong DC, Quinn PV, Luding S. 2001. Reverse Brazil nut problem: Competition between percolation and condensation. Phys Rev Lett. 86(15):3423–3426. https://doi.org/10.1103/PhysRevLett.86.3423

Houston R, Oyedeji O, Abdoulmoumine N. 2022. Detailed biomass fast pyrolysis kinetics integrated to computational fluid dynamic (CFD) and discrete element modeling framework: Predicting product yields at the bench-scale. Chem Eng-New Y J. 444:136419. https://doi.org/10.1016/j.cej.2022.136419

Jaeger B. 2024. DEM/CFD-Simulationen der Wärme- und Stoffübertragung eines mit Gas durchströmten Festbettes aus komplex geformten, pyrolysierenden Holzpartikeln. Bochum: Ruhr-University Bochum.

Jaeger B, Illana Mahiques E, Wirtz S, Scherer V. 2023. Pyrolysis of spherical wood particles in a packed bed – comparison between resolved and unresolved discrete element method/computational fluid dynamics. Chem Eng Technol. 46(10):2120–2132. https://doi.org/10.1002/ceat.202300266

Kalderon M, Smith E, O'Sullivan C. 2022. Comparative analysis of porosity coarse-graining techniques for discrete element simulations of dense particulate systems. Comput Particle Mech. 9 (1):199–219. https://doi.org/10.1007/s40571-021-00402-4

Mahmoudi AH, Besseron X, Hoffmann F, Markovic M, Peters B. 2016. Modeling of the biomass combustion on a forward acting grate using XDEM. Chem Eng Sci. 142:32–41. https://doi.org/10.1016/j.ces.2015.11.015

Mahmoudi AH, Hoffmann F, Peters B, Besseron X. 2016. Numerical study of the influence of particle size and packing on pyrolysis products using XDEM. Int Commun Heat Mass Transf. 71:20–34. https://doi.org/10.1016/j.icheatmasstransfer.2015.12.011

OpenCFD Ltd. 2024. OpenFOAM Documentation. https://doc.openfoam.com/2312/tools/processing/solvers/rtm/combustion/fireFoam/

Peters B, Schröder E, Bruch C. 2003. Measurements and particle resolved modelling of the thermo- and fluid dynamics of a packed bed. J Analytical Appl Pyrolysis. 70(2):211–231. https://doi.org/10.1016/S0165-2370(02)00133-X

Porteiro J et al. 2010. Experimental analysis of the ignition front propagation of several biomass fuels in a fixed-bed combustor. Fuel. 89(1):26–35. https://doi.org/10.1016/j.fuel.2009.01.024

Rönnbäck M, Axell M, Gustavsson L, Thunman H, Lecher B. 2001. Combustion processes in a biomass fuel bed-experimental results. In: Bridgwater AV, editor. Progress in thermochemical biomass conversion. Wiley; pp 743–757. https://doi.org/10.1002/9780470694954.ch59

Sadhukhan AK, Gupta P, Saha RK. 2008. Modelling and experimental studies on pyrolysis of biomass particles. J Analytical Appl Pyrolysis. 81(2):183–192. https://doi.org/10.1016/j.jaap.2007.11.007

Shin D, Choi S. 2000. The combustion of simulated waste particles in a fixed bed. Combust Flame. 121(1–2):167–180. https://doi.org/10.1016/S0010-2180(99)00124-8

Simsek E, Sudbrock F, Wirtz S, Scherer V. 2012. Influence of particle diameter and material properties on mixing of monodisperse spheres on a grate: Experiments and discrete element simulation. Powder Technol. 221:144–154. https://doi.org/10.1016/j.powtec.2011.12.051

Sudbrock F, Simsek E, Wirtz S, Scherer V. 2010. An experimental analysis on mixing and stoking of monodisperse spheres on a grate. Powder Technol. 198(1):29–37. https://doi.org/10.1016/j.powtec.2009.10.011

Van Der Lans RP, Pedersen LT, Jensen A, Glarborg P, Dam-Johansen K. 2000. Modelling and experiments of straw combustion in a grate furnace. Biomass Bioenerg. 19(3):199–208. https://doi.org/10.1016/S0961-9534(00)00033-7

Van Kessel LBM, Arendsen ARJ, De Boer-Meulman PDM, Brem G. 2004. The effect of air preheating on the combustion of solid fuels on a grate. Fuel. 83(9):1123–1131. https://doi.org/10.1016/j.fuel.2003.11.008

Vargas WL, McCarthy JJ. 2001. Heat conduction in granular materials. AlChE J. 47(5):1052–1059. https://doi.org/10.1002/aic.690470511

Vargas WL, McCarthy JJ. 2002. Conductivity of granular media with stagnant interstitial fluids via thermal particle dynamics simulation. Int J Heat Mass Transf. 45(24):4847–4856. https://doi.org/10.1016/S0017-9310(02)00175-8

Wang J, Ku X, Yang S. 2022. Simulation of biomass pyrolysis in a rotary drum by coupling CFD-DEM with a one-dimensional thermally thick model. Energy Fuels. 36(7):3665–3679. https://doi.org/10.1021/acs.energyfuels.2c00050

Wenzl HFJ. 1970. The chemical technology of wood. Academic Press.

Wiese J et al. 2016. Dem/CFD modeling of the fuel conversion in a pellet stove. Fuel Process Technol. 152:223–239. https://doi.org/10.1016/j.fuproc.2016.06.005

Wissing F, Wirtz S, Scherer V. 2017. Simulating municipal solid waste incineration with a DEM/CFD method – influences of waste properties, grate and furnace design. Fuel. 206:638–656. https://doi.org/10.1016/j.fuel.2017.06.037

Xia C et al. 2021. A review on the modeling and validation of biomass pyrolysis with a focus on product yield and composition. Biofuel Res J. 8(1):1296–1315. https://doi.org/10.18331/BRJ2021.8.1.2

Yang YB, Sharifi VN, Swithenbank J. 2004. Effect of air flow rate and fuel moisture on the burning behaviours of biomass and simulated municipal solid wastes in packed beds. Fuel. 83(11–-12):1553–1562. https://doi.org/10.1016/j.fuel.2004.01.016

Yin C, Li S. 2017. Advancing grate-firing for greater environmental impacts and efficiency for decentralized biomass/wastes combustion. Energy Procedia. 120:373–379. https://doi.org/10.1016/j.egypro.2017.07.220

Zhang X, Chen Q, Bradford R, Sharifi V, Swithenbank J. 2010. Experimental investigation and mathematical modelling of wood combustion in a moving grate boiler. Fuel Process Technol. 91(11):1491–1499. https://doi.org/10.1016/j.fuproc.2010.05.026

Appendix

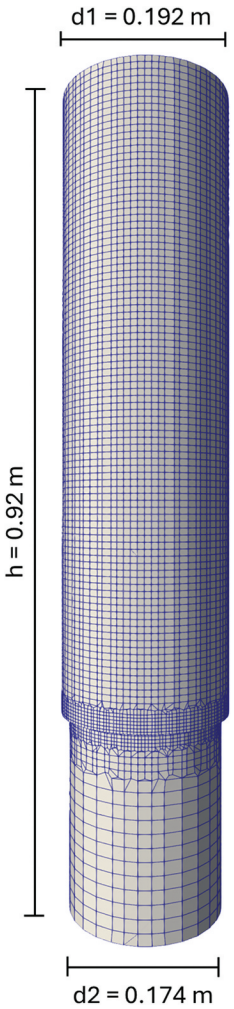

Figure A1. CFD mesh of the reactor set up.

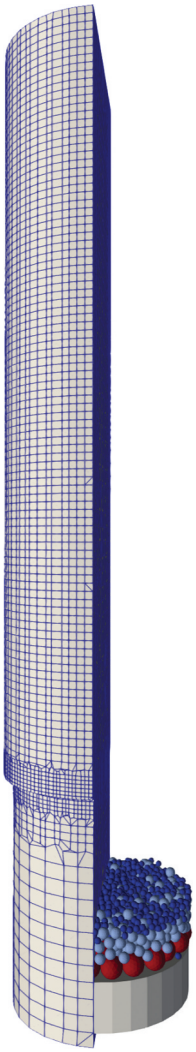

Figure A2. Particle bed in the reactor set up.

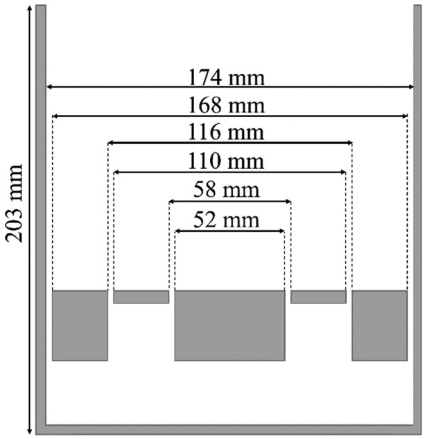

Figure A3. Schematic diagram and measurements of the burner bowl with stoking elements in their initial position.

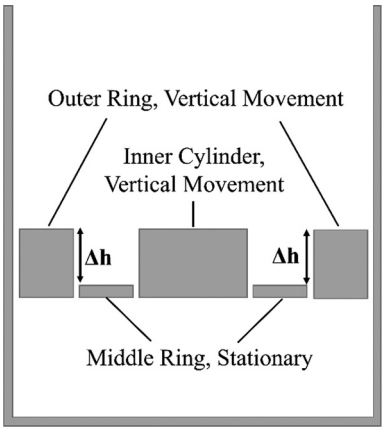

Figure A4. Schematic diagram of the burner bowl with stokingelements at stroke length of Δh = 20 mm.

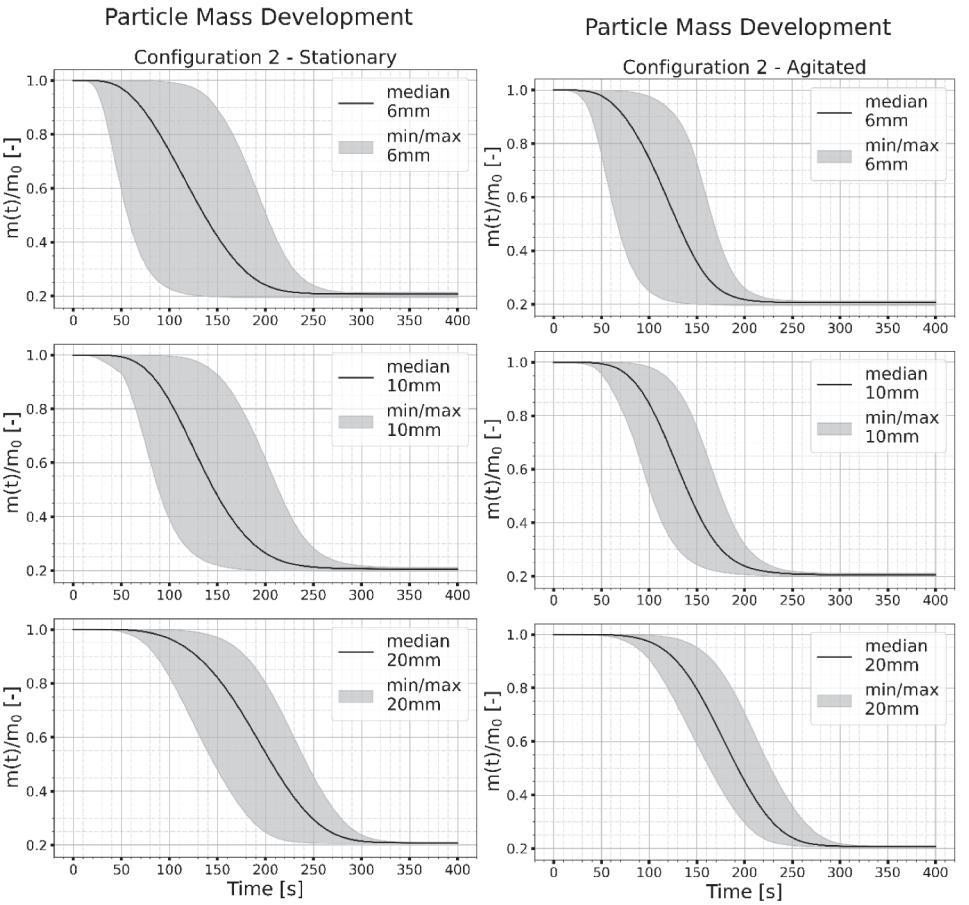

a. Absolute mass over time for configuration 2, stationary

b. Absolute mass over time for configuration 2, agitated

Figure A5. (a) Absolute mass over time for configuration 2, stationary. (b) Absolute mass over time for configuration 2, agited.